PHYSICAL REVIEW D VOLUME 44, NUMBER 10 15 NOVEMBER 1991

Initial data for axisymmetric black-hole collisions

Gregory B. Cook
Center for Radiophysics and Space Research
and Center for Theory and Simulation in Science and Engineering, Cornell University, Ithaca, New York 14853
(Received 8 July 1991)

The construction of initial-data sets to be used in the simulation of black-hole collisions is studied in the context of the conformal-imaging formalism. An approach is described for evaluating a formal, infinite-series solution of the momentum-constraint equation. This solution allows for the construction of completely general three-dimensional configurations of two black holes with individually specifiable linear and angular momenta. Using this solution for the momentum constraint, the Hamiltonian constraint is solved numerically in the restricted case of axisymmetric configurations. Two codes for solving the Hamiltonian constraint are described, one based on bispherical coordinates and the other on Čadež coordinates. The accuracies of the numerical solutions are gauged by comparison with analytic results, Richardson extrapolation, and comparison of the results from the two codes. Finally, the physical content of data sets representing two equal-sized holes with linear or angular momenta is explored. The results show several expected physical effects including the gravitational spin-spin interaction.

I. INTRODUCTION

The strong-field, fully relativistic two-body problem remains one of the most important unsolved problems in the field of general relativity. In addition to representing what is arguably the most fundamental dynamical interaction in any theory of gravity, the two-body problem is of great interest in the expanding search for gravitational waves. While aspects of the two-body problem can be studied through weak-field or perturbative techniques, numerical techniques remain as the only avenue for study of the most interesting, fully relativistic, strong-field situations. The numerical study of the two-body problem is a complex, multifaceted endeavor. In this paper, I will describe efforts directed at one aspect of the problem: the generation of initial-data sets which can be used to investigate the collision of two black holes.

To date, the numerical study of the collision of black holes has been limited to evolutions which have started from time-symmetric initial data where the holes start out at rest from a finite separation [1–3]. The initial data used to start these simulations were formulated by Misner [4] and are one of the few known *analytic* solutions of the initial-value equations. Collisions resulting from these initial data are, of course, head-on. While such a collision will result in the emission of gravitational waves, it is believed that non-head-on, spiraling collisions will be more efficient sources of gravitational waves and will certainly be more common. In order to simulate such collisions, initial-data sets must be constructed which can represent black holes with some initial linear (and angular) momenta.

A framework has been erected which is designed to allow for the construction of initial-data sets containing multiple black holes, each with individually specifiable linear and angular momenta [5–9]. This approach, sometimes called the conformal-imaging approach, is based on the $3+1$ decomposition of Einstein's equations, York's conformal and transverse-traceless decompositions of the constraint equations, and a method of imaging applicable to tensors. The conformal-imaging method has been used extensively to study initial-data sets for the case of a single black hole with linear and angular momenta [10–12]. The application of the method to the case of two black holes was first attempted by Bowen *et al.* [13] and Rauber [14], who were able to evaluate the formal solution of Kulkarni *et al.* [9] for the momentum-constraint equations in the context of a restricted set of configurations. However, their attempts to find numerical solutions to the Hamiltonian constraint were unsuccessful. Thornburg [15], using a related approach, demonstrated the feasibility of solving the Hamiltonian constraint for initial-data sets containing two black holes.

In this paper, I will describe a completely general approach for evaluating the formal solution of the momentum-constraint equations of Kulkarni *et al.* [9] for the case of two holes. This general approach incorporates a parametrization of the location and relative sizes of black holes in the initial-data slice and allows for associating completely arbitrary linear and angular momenta with each hole. Further, I will describe the construction of complete initial-data sets by numerically solving the Hamiltonian constraint in the restricted domain of axisymmetry. The resulting solutions will be completely consistent with the conformal-imaging formalism. To verify the accuracy of the numerical solutions, two separate codes have been developed to solve the Hamiltonian constraint. The first code relies on a discretization of the computational domain based on bispherical coordinates. The discretization in the second code is based on a numerically generated coordinate system which is referred to as Čadež coordinates. This coordinate system is espe-

cially well adapted for investigating the collision of two black holes and was used by Čadež [1] and later by Smarr and Eppley [2,3] in their investigations of black-hole collisions. While especially well adapted to the two-body problem, it has proven to be somewhat difficult to work with. I will show, however, that the Čadež coordinate system can be used successfully to generate accurate numerical solutions of the Hamiltonian constraint equation. The accuracy of solutions found by both codes has been investigated using Richardson-extrapolation techniques and the extrapolated solutions of both codes have been compared to lend further support to the high accuracy of the solutions.

Much of the physical content of these initial-data sets cannot be specified in, but rather must be derived from, the initial data. In light of this, the physical content of the initial-data sets will be explored. Because the locations of all of the trapped surfaces which will be present in these data sets have not been determined, the analysis of the physical content and the causal structure is preliminary. A more complete analysis of the physical and causal structure of these initial-data sets will be presented in a future paper [16].

In this work, I will begin with a brief review of the conformal-imaging formalism for multiple black holes with linear and angular momenta. Next, I will describe the numerical evaluation of the formal solution of the momentum-constraint equation. Using this solution, I next explore approaches and techniques for solving the Hamiltonian-constraint equation and describe the results from two numerical codes for solving the Hamiltonian constraint in the restricted domain of axisymmetry. I will conclude with a preliminary investigation of the physical content of the initial-data sets and a discussion of future work.

II. THE CONFORMAL-IMAGING FORMALISM

The Arnowitt-Deser-Misner [17] (ADM) or 3 + 1 decomposition of Einstein's equations and York's conformal decomposition of the constraint equations [5] provide a well-proven foundation for specifying initial-data sets for a wide range of problems of astrophysical and cosmological interest. The vacuum Hamiltonian and momentum constraints can be expressed, respectively, as

$$8\bar{\nabla}^2\psi - \psi\bar{R} - \frac{2}{3}\psi^5 K^2 + \psi^{-7}\bar{A}_{ij}\bar{A}^{ij} = 0 \tag{1}$$

and

$$\bar{D}_j\bar{A}^{ij} - \frac{2}{3}\psi^6\bar{\gamma}^{ij}\bar{D}_j K = 0. \tag{2}$$

The physical metric γ_{ij} of the spacelike initial-data hypersurface has been conformally decomposed to $\gamma_{ij} = \psi^4\bar{\gamma}_{ij}$, where ψ is a strictly positive conformal factor and $\bar{\gamma}_{ij}$ is the conformal *background* metric. The extrinsic curvature K_{ij}, describing the embedding of the initial-data hypersurface in the full space-time, has also been decomposed as $K_{ij} = \psi^{-2}\bar{A}_{ij} + \frac{1}{3}\gamma_{ij}K$, where K is the trace of the extrinsic curvature and $\bar{A}_{ij}$ is the trace-free conformal *background* extrinsic curvature. Finally, $\bar{R}$ is the Ricci scalar, $\bar{D}_i$ is the covariant derivative, and $\bar{\nabla}^2$ is the scalar Laplacian, all compatible with the conformal background metric. Note that all quantities with an overbar exist in the conformal background space and are related to similar quantities (without overbars) which exist in the physical space.

To simplify the task of solving these equations, the following choices are made. First, the initial-data hypersurface is taken to be maximally embedded in the space-time so that $K = 0$. Second, the initial-data hypersurface is taken to be conformally flat so that $\bar{\gamma}_{ij} = f_{ij}$, a flat metric. This choice fixes the dynamical degrees of freedom in the metric on the initial hypersurface and simplifies both the Hamiltonian and momentum constraints. With these assumptions, the initial-value equations reduce to the simple form

$$\bar{\nabla}^2\psi = -\frac{1}{8}\psi^{-7}\bar{A}_{ij}\bar{A}^{ij} \tag{3}$$

and

$$\bar{D}_j\bar{A}^{ij} = 0. \tag{4}$$

Note that $\bar{D}_i$ and $\bar{\nabla}^2$ are now the familiar flat-space covariant derivative and scalar Laplacian.

The final assumptions of the conformal-imaging approach are concerned with fixing the topology of the initial-data hypersurface. Recall that the topology of space-time is not determined by Einstein's equations and so must be given. The first assumption is that the hypersurface be asymptotically flat. This is a natural assumption as we are interested in isolated black-hole systems. The final assumption and its consequences lie at the heart of the conformal-imaging formalism and are not so straightforward. Because we wish to model black holes in a vacuum, and thus have no sources to support a nontrivial, conformally flat gravitational field, we are forced to choose an initial-data hypersurface with a nontrivial topology. As is familiar from a t = const slice of the Schwarzschild geometry in isotropic coordinates, the initial-data hypersurface for a single black hole consists of *two* asymptotically flat "sheets" connected by a throat or Einstein-Rosen bridge [18]. There is no unique generalization of this topology for the case of multiple black holes, but there are two basic generalizations [19]. First, one can consider N black holes in one "universe," or sheet, to be connected through a throat to its own unique asymptotically flat sheet. This produces a manifold with $N+1$ sheets. The second basic generalization is to have all N holes in one universe connected via throats to the same second asymptotically flat sheet. This produces a two-sheeted manifold. A hybrid of these two general topologies is, of course, possible in the case of three or more holes. In the conformal-imaging formalism the two-sheeted manifold structure is chosen along with the additional demand that the two sheets be related by an isometry so that the physical fields in the two sheets are "identical" [4, 9, 19]. This two-sheeted structure, along with the identification of the two sheets, is the most faithful generalization of the Schwarzschild geometry to the case of multiple holes. To see this, it is

necessary to examine the form of the isometry condition.

Following Kulkarni *et al.* [9], let $J^i_\alpha(x)$ denote a coordinate map which identifies points in the two sheets through the αth throat. The demand that the two sheets be isometric then forces certain conditions on the physical fields in the hypersurface. Most important at present are the conditions placed on the physical metric and extrinsic curvature. These conditions are

$$\gamma_{ij}(x) = (J_\alpha)^k_i (J_\alpha)^\ell_j \gamma_{k\ell}(J_\alpha(x)) \tag{5}$$

and

$$K_{ij}(x) = \pm (J_\alpha)^k_i (J_\alpha)^\ell_j K_{k\ell}(J_\alpha(x)). \tag{6}$$

Here, $(J_\alpha)^i_j = \partial J^i_\alpha / \partial x^j$ is the Jacobian of the αth coordinate map.

Following Misner [4], Kulkarni *et al.* [9] take the coordinate maps to be defined by inversion through a sphere. This is the same isometry condition obeyed by the Schwarzschild geometry (in isotropic coordinates), and it is in this sense that the present choice of topology is the most direct generalization of the Schwarzschild geometry. In terms of Cartesian coordinates, the coordinate maps can be expressed as

$$J^i_\alpha(x) \equiv \left(\frac{a^2_\alpha}{r_\alpha}\right) n^i_\alpha + C^i_\alpha, \tag{7}$$

where $r_\alpha = |x^i - C^i_\alpha|$, $n^i_\alpha = (x^i - C^i_\alpha)/r_\alpha$, and a_α and C^i_α are, respectively, the radius and center of the αth throat in the flat background space.

In terms of this explicit form for the inversion maps, the following conditions are imposed on the conformal factor and background extrinsic curvature:

$$\begin{aligned}\psi(x) &= \mathcal{N}_\alpha \circ \psi(x) \\ &= \frac{a_\alpha}{r_\alpha} \psi(J_\alpha(x))\end{aligned} \tag{8}$$

and

$$\begin{aligned}\bar{A}_{ij}(x) &= \mathcal{R}^\pm_\alpha \circ \bar{A}_{ij}(x) \\ &= \pm \left(\frac{a_\alpha}{r_\alpha}\right)^2 (J_\alpha)^k_i \bar{A}_{k\ell}(J_\alpha(x))(J_\alpha)^\ell_j.\end{aligned} \tag{9}$$

These conditions are completely compatible with the constraint equations. More precisely, if the conformal factor and background extrinsic curvature satisfy these conditions [(8) and (9)] (they are said to be inversion symmetric if they do) and if they satisfy the constraint equations (3) and (4) in one of the sheets, then they are guaranteed to satisfy the constraints in the second sheet.

III. THE MOMENTUM CONSTRAINT

Solving the momentum constraint is the first step in constructing inversion-symmetric initial-data sets. Since the initial hypersurface is maximally embedded in the space-time, the momentum-constraint equation decouples from the conformal factor. This is one of the prime strengths of the conformal decomposition of the constraints and can be exploited in certain cases to find analytic solutions for the background extrinsic curvature. Further, because the initial data are constructed to be conformally and asymptotically flat, one can determine, *without solving the Hamiltonian constraint*, the total *physical* linear momentum

$$P^i = \frac{1}{8\pi} \oint_\infty \bar{A}^{ij} d^2 \bar{S}_j \tag{10}$$

and total *physical* angular momentum content

$$S_i = \frac{\epsilon_{ijk}}{8\pi} \oint_\infty x^j \bar{A}^{k\ell} d^2 \bar{S}_\ell \tag{11}$$

of the resulting initial data [7]. Note that these integrals are in terms of *Cartesian* coordinates.

In the context of the conformal-imaging formalism, the construction of initial-data sets containing black holes with linear and angular momenta has been greatly facilitated by a set of analytic, inversion-symmetric solutions of the momentum constraint found by Bowen and York [7] for the case of a single hole. There are two solutions $\bar{A}^\pm_{ij}$ which carry linear momentum P_i:

$$\begin{aligned}\bar{A}^\pm_{ij} = &\frac{3}{2r^2}\left[P_i n_j + P_j n_i - (f_{ij} - n_i n_j) P^k n_k\right] \\ &\mp \frac{3a^2}{2r^4}\left[P_i n_j + P_j n_i + (f_{ij} - 5 n_i n_j) P^k n_k\right].\end{aligned} \tag{12}$$

a is the radius of the throat of the hole in the conformal background space, r is the radial distance from the origin, and n^i is the unit normal of a sphere. The solution $\bar{A}^+_{ij}$ satisfies isometry condition (9) with the plus sign, and $\bar{A}^-_{ij}$ satisfies isometry condition (9) with the minus sign. There is also a solution $\bar{A}^s_{ij}$ which carries angular momentum S_i:

$$\bar{A}^s_{ij} = \frac{3}{r^3}(\epsilon_{ki\ell} S^\ell n^k n_j + \epsilon_{kj\ell} S^\ell n^k n_i). \tag{13}$$

This solution satisfies isometry condition (9) with the minus sign. (There is no one-hole solution carrying angular momentum which satisfies the isometry condition with a plus sign.) Solutions of the Hamiltonian constraint using (12) and (13) have been extensively explored by many researchers [10–12].

The problem of constructing a multihole, inversion-symmetric solution of the momentum constraint has been addressed by Kulkarni *et al.* [9]. The approach is centered on the fact that the momentum constraint (4) is linear. Since this is the case, a solution representing N black holes, each with linear and angular momenta, can be obtained from (12) and (13) as

$$\begin{aligned}\bar{A}_{ij} = 3 \sum_{\alpha=1}^{N} \Bigg(&\frac{1}{2r^2_\alpha}\left[P^\alpha_i n^\alpha_j + P^\alpha_j n^\alpha_i - (f_{ij} - n^\alpha_i n^\alpha_j) P^k_\alpha n^\alpha_k\right] \\ &+ \frac{1}{r^3_\alpha}(\epsilon_{ki\ell} S^\ell_\alpha n^k_\alpha n^\alpha_j + \epsilon_{kj\ell} S^\ell_\alpha n^k_\alpha n^\alpha_i)\Bigg).\end{aligned} \tag{14}$$

Note that the second term in (12) has been omitted here. The N black holes are given individual linear and angular momenta P^i_α and S^i_α in the sense that if the holes are

"sufficiently far apart," they will have such momenta as measured by (10) and (11). If the holes are close together, then all that can be measured is the total linear and angular momenta of the system.

While (14) represents a multihole solution to the momentum constraint, it does not satisfy isometry condition (9). Including the omitted second term in (12) within (14) does not change this. Even though (14) is not inversion symmetric, Kulkarni *et al.* [9] have shown how to take such a non-inversion-symmetric extrinsic curvature and make it inversion symmetric through a method of images applicable to tensors. When there is more than one hole, this procedure results in an infinite number of imaging terms being added to the "base" extrinsic curvature.

Consider the operator $\mathcal{R}^{\pm}_{\alpha}$ for imaging through the αth hole defined in (9). As Kulkarni *et al.* [9] have shown, this operator is its own inverse, $\mathcal{R}^{\pm}_{\alpha} \circ \mathcal{R}^{\pm}_{\alpha} = \mathbb{1}$. Also, if this operator acts upon a symmetric, second-rank, divergenceless tensor, the result is a symmetric, second-rank, divergenceless tensor. Now consider the operator

$$\mathcal{R}^{\pm} = \mathbb{1} + \sum_{\{\alpha_i\}} \left(\prod_{i=1}^{m} \mathcal{R}^{\pm}_{\alpha_i} \right). \tag{15}$$

The label α_i takes on values of $1, \ldots, N$. The sum is over all unique sequences $\{\alpha_i\}$ of length m, where a sequence is unique only if $\alpha_i \neq \alpha_{i+1}$. For any sequence, $\{\alpha_i\}$, one takes a product of "image" operators corresponding to that sequence. For example, if $N = 2$, then

$$\begin{aligned}\mathcal{R}^{\pm} = \mathbb{1} &+ \mathcal{R}^{\pm}_1 + \mathcal{R}^{\pm}_1 \circ \mathcal{R}^{\pm}_2 + \mathcal{R}^{\pm}_1 \circ \mathcal{R}^{\pm}_2 \circ \mathcal{R}^{\pm}_1 + \cdots \\ &+ \mathcal{R}^{\pm}_2 + \mathcal{R}^{\pm}_2 \circ \mathcal{R}^{\pm}_1 + \mathcal{R}^{\pm}_2 \circ \mathcal{R}^{\pm}_1 \circ \mathcal{R}^{\pm}_2 + \cdots .\end{aligned} \tag{16}$$

It is easy to verify that $\mathcal{R}^{\pm}_{\alpha} \circ \mathcal{R}^{\pm} = \mathcal{R}^{\pm}$ for all α. Thus, if (15) acts on any arbitrary, symmetric, trace-free, divergenceless tensor, the result will be an *inversion-symmetric*, symmetric, trace-free, divergenceless tensor.

The formal approach for obtaining an inversion-symmetric solution to the momentum constraint (4) is now obvious. Let $\hat{A}_{ij}$ represent an appropriately weighted sum of single-hole solutions to the momentum constraint. The inversion-symmetric solution is then given by

$$\bar{A}_{ij} = \mathcal{R}^{\pm} \circ \hat{A}_{ij}. \tag{17}$$

Kulkarni [20] has shown that for any reasonable choice for $\hat{A}_{ij}$, the infinite series converges if the holes are far enough apart. In particular, if there are just two holes, then the infinite series converges absolutely, provided that the inversion surfaces do not overlap.

If we wish for P^i_{α} and S^i_{α} to represent the physical linear and angular momenta of the holes, then the appropriate form for $\hat{A}_{ij}$ is

$$\begin{aligned}\hat{A}_{ij} = \frac{3}{2} \sum_{\alpha=1}^{N} \Bigg(&\frac{1}{r^2_{\alpha}} \left[P^{\alpha}_i n^{\alpha}_j + P^{\alpha}_j n^{\alpha}_i - (f_{ij} - n^{\alpha}_i n^{\alpha}_j) P^k_{\alpha} n^{\alpha}_k \right] \\ &+ \frac{1}{r^3_{\alpha}} (\epsilon_{ki\ell} S^{\ell}_{\alpha} n^k_{\alpha} n^{\alpha}_j + \epsilon_{kj\ell} S^{\ell}_{\alpha} n^k_{\alpha} n^{\alpha}_i) \Bigg).\end{aligned} \tag{18}$$

Note that (18) differs from (14) by a factor of $\frac{1}{2}$ in the angular momentum terms. This factor is included because (13) is its own image term. As seen from (12), the self-image term of a linear momentum term behaves asymptotically as $O(r^{-4})$ and carries no linear or angular momenta. A tedious, explicit calculation shows that all other "general"-image terms have a leading behavior of $O(r^{-6})$ and again carry no linear or angular momenta. Thus, we find that the total physical linear momentum contained in the initial-data slice is simply $\sum_{\alpha} P^i_{\alpha}$, and the total physical angular momentum is given by $\sum_{\alpha} S^i_{\alpha}$+(orbital angular momentum terms) arising from the linear momenta of the holes.

In order to find solutions to the Hamiltonian constraint and thus construct complete initial-data sets, it is necessary to move past the formalism described above and find a concrete method for computing the inversion-symmetric extrinsic curvature. This problem was first investigated by Bowen *et al.* [13] for the case of axisymmetric spinning holes where the holes are of equal size and have equal magnitude momenta on each hole. They were able to find an analytic expression for each term in the infinite series for any number of holes. Unfortunately, if their approach is expanded to include linear momentum in the axisymmetric case or if nonaxisymmetric configurations are attempted, certain recursive relationships are lost and the approach becomes intractable. The apparent difficulty in evaluating an inversion-symmetric solution to the momentum constraint for multiple holes has been considered a major hindrance to the use of the conformal-imaging approach.

Fortunately, a simple solution exists if there is no need for a full analytic expression for the solution of the momentum constraint [21]. If only a numerical value for the components of $\bar{A}_{ij}$ is needed, then the infinite-series solution of (17) can be rewritten in terms of a small set of recursively defined quantities. In this paper, we are specifically interested in the case of two holes. In this case, (17) can be rewritten as

$$\begin{aligned}\bar{A}_{ij}(x) &= \mathcal{R}^{\pm} \circ \hat{A}_{ij}(x) \\ &= \hat{A}_{ij}(x) \\ &\quad + \sum_{n=1}^{\infty} (\pm 1)^n [F^n_1 (M^n_1)^k_i (\hat{A}_{k\ell})_{(x^n_1)} (M^n_1)^{\ell}_j \\ &\qquad + F^n_2 (M^n_2)^k_i (\hat{A}_{k\ell})_{(x^n_2)} (M^n_2)^{\ell}_j].\end{aligned} \tag{19}$$

The definitions of the recursively defined quantities x^n_1, x^n_2, $(M^n_1)^j_i$, $(M^n_2)^j_i$, F^n_1, and F^n_2 are given in Appendix A. What should be noted is that the evaluation of the nth term in the series involves *only* the value of the six recursively defined quantities of the $(n-1)$th term and, further, involves only simple arithmetic operations so that it is computationally inexpensive to evaluate (compared to the evaluation of a given term via the approach of Bowen *et al.* [13]).

The method described above and detailed in Appendix A allows for the construction of completely general, three-dimensional, inversion-symmetric solutions of

the momentum-constraint equation. The two holes can be assigned any desired linear or angular momenta and can, for example, represent two holes in a bound orbit which will lead to a spiraling coalescence of black holes. All that remains in the construction of complete inversion-symmetric initial-data sets is to find solutions of the Hamiltonian constraint. This problem will be considered next.

IV. THE HAMILTONIAN CONSTRAINT

The final step in the construction of initial-data sets via the conformal-imaging approach is the solution of the Hamiltonian constraint (3). As described in Sec. II, the isometry relating the two sheets of the initial-data hypersurface allows that a solution need be found in only one of the sheets. In the background space, the domain of a sheet is the region of the Euclidean three-space exterior to each of the throats. If proper boundary conditions can be posed on these throats and at infinity, then the Hamiltonian constraint can be posed as a quasilinear, elliptic boundary-value problem. Bowen and York [7] have derived such boundary conditions, and these will be described below. I will also discuss a general asymptotic expansion for solutions to the Hamiltonian constraint when the inversion-symmetric extrinsic curvature has the form given by (17) and (18).

In order for a solution of the Hamiltonian constraint to be inversion symmetric, it must satisfy isometry condition (8) for every hole in the system. This set of isometry conditions defines boundary conditions which, when imposed at the throats, guarantee that a solution obeys the isometry conditions. These conditions

$$n^i_\alpha \bar{D}_i \psi \Big|_{a_\alpha} = -\frac{\psi}{2r_\alpha}\Big|_{a_\alpha} \tag{20}$$

are derived directly from isometry condition (8) by contracting the gradient of this equation with the unit normal to the surface and using the fact that the inversion surface is a fixed-point set of the isometry. This formulation of the boundary conditions reduces directly to that derived by Bowen and York [7] for a single hole and by Kulkarni *et al.* [9] for the case of multiple holes. The boundary condition at infinity follows directly from asymptotic and conformal flatness:

$$\psi \to 1 \quad \text{as } r \to \infty. \tag{21}$$

In practice, infinity is often not part of the domain of solution for the conformal factor when numerical solutions are found. If this is the case, then an approximate boundary condition must be used at large distances from the holes. York and Piran [10] have proposed and used an approximate boundary condition based on an asymptotic expansion of the conformal factor. This boundary condition was truncated at monopole order because, in general, the dipole term in the expansion of the conformal factor is not well defined. However, if the extrinsic curvature term in the Hamiltonian constraint takes the form given by (17) and (18), then the expansion *can* be extended at least to dipole order [21].

Following Bowen *et al.* [13], consider the Hamiltonian constraint written in terms of a "Newtonian" potential $\Phi = 2(1-\psi)$:

$$\bar{\nabla}^2 \Phi = \frac{1}{4}\psi^{-7}\bar{A}_{ij}\bar{A}^{ij} \equiv 4\pi\rho_{\text{eff}}, \tag{22}$$

where ρ_{eff} is defined as an effective energy-density source. It is the falloff behavior of this source which will determine the properties of any multipole expansion of Φ. Asymptotic flatness requires that $\rho_{\text{eff}} = O(r^{-4})$, and so the series expansion is always well defined through monopole order. An asymptotic expansion of the background extrinsic curvature given in (17) and (18) shows that if there is a nonzero *net* linear momentum for the configuration, then the effective energy density will in fact fall off as $O(r^{-4})$. In spite of this, it is possible to extend the asymptotic expansion to include the dipole term by adding a correction to the multipole expansion which will cancel the leading-order terms in the effective energy density. The resulting asymptotic expansion, expressed in terms of the conformal factor, is

$$\psi = 1 + \frac{1}{2}\left(\frac{E}{r} + \frac{d_i n^i}{r^2} - \frac{9}{16r^2}\sum_{\alpha=1}^{N}\sum_{\beta=1}^{N}\left(P^\alpha_i P^i_\beta - 2P^\alpha_i n^i P^\beta_j n^j\right)\right) + O(r^{-3}), \tag{23}$$

where n^i is the unit normal to a sphere centered at $r = 0$. E and d_i are the usual monopole and dipole moments of the energy distribution given by the integrals

$$E = -\frac{1}{2\pi}\oint_\infty \bar{D}^i\psi d^2\bar{S}_i \tag{24}$$

and

$$d_i = -\frac{1}{2\pi}\oint_\infty [x_i\bar{D}^j\psi + (1-\psi)\delta^j_i]d^2\bar{S}_j. \tag{25}$$

Note that the integral for the dipole moment is in terms of Cartesian components. The standard integrals for these multipole moments hold and, in particular, the dipole order is well defined because the correction term contributes nothing to the dipole moment.

A boundary condition based on (23) can be obtained by taking a radial derivative of this equation and then

eliminating the monopole term. The result is

$$\frac{\partial\psi}{\partial r} = \frac{1-\psi}{r} - \frac{1}{2r^3}\left(d_i n^i - \frac{9}{16}\sum_{\alpha=1}^{N}\sum_{\beta=1}^{N}\left(P_i^\alpha P_\beta^i - 2P_i^\alpha n^i P_j^\beta n^j\right)\right) + \frac{1}{r}O(r^{-3}). \tag{26}$$

The term in large parentheses is the extension to the boundary condition of York and Piran [10]. This addition is an improvement if it is either impossible or inconvenient to use a center-of-energy and center-of-momentum coordinate system. The presence of the dipole moment in (26) means that this boundary condition must be imposed iteratively in numerical schemes. However, because the dipole term occurs at one order in r below the dominant term, it will constitute only a small correction and the iterative scheme will converge.

Before restricting attention to the case of two holes, it should be mentioned that an exact, inversion-symmetric solution to the Hamiltonian constraint exists. In the case of time symmetry ($K_{ij} = 0$), the Hamiltonian constraint is linear, and Misner [4] has constructed a formal inversion-symmetric solution for the case of N holes. This solution can be numerically evaluated and is used as a test case in evaluating numerical solution schemes. Appendix B describes a method for evaluating the series for the case of two holes with arbitrary relative sizes and separations.

A general configuration of the two holes is described by three quantities: the radii of each hole a_1 and a_2, and the separation of the centers of the two holes $|C_1^i - C_2^i|$. It will be convenient to work in terms of dimensionless quantities, and so I will choose the radius of the first hole to set the length scale of the problem. A general configuration is then parametrized by two quantities:

$$\alpha = \frac{a_1}{a_2} \tag{27}$$

and

$$\beta = \frac{|C_1^i - C_2^i|}{a_1}. \tag{28}$$

To proceed with a numerical investigation of solutions to the Hamiltonian constraint, an appropriate coordinate system must be chosen. In order to impose the inversion-symmetry boundary conditions, it is desirable that a coordinate system have constant coordinate surfaces which coincide with the throats. Bispherical coordinates are a natural choice to satisfy this requirement and prove to be an excellent choice for solving for the initial data because the coordinate system includes spatial infinity in a finite coordinate space. This allows the boundary condition for asymptotic flatness to be imposed as a Dirichlet boundary condition. Unfortunately, the bispherical coordinate system becomes very distorted at large distances from the holes and this behavior makes them ill suited for use in an evolution of the initial data.

Considering the eventual evolution of these initial-data sets, it would be desirable for the coordinate system to approach spherical coordinates at large distances from the holes. This behavior will facilitate the outward propagation of gravitational waves on the grid and ease the task of formulating outer boundary conditions. A coordinate system with this behavior and which has constant coordinate surfaces coincident with the throats can be constructed numerically using a complex-plane transformation and was first used by Čadež [1] in his early investigations into black-hole collisions. The definition of these coordinates is given in Appendix C. The requirement of constant coordinate surfaces surrounding the throats both individually and collectively necessitates the presence of a coordinate singularity in the region between the two holes. This fact complicates the use of these coordinates but the difficulties can be handled.

In the next two sections I will describe two approaches for solving the Hamiltonian constraint, one based on bispherical coordinates and one based on Čadež coordinates. The bispherical scheme will be examined first because the coordinate system is well behaved and is robust in the configurations it can handle, aiding in the testing of numerical results. Solutions from the bispherical scheme can then be used to test the accuracy of solutions to the Čadež scheme.

V. THE BISPHERICAL SCHEME

Using cylindrical coordinates as a starting point, a two-hole configuration can be oriented so that the centers of both holes lie on the z axis. The coordinate transformations to bispherical coordinates are then

$$\rho = \frac{C\sin\xi}{\cosh\eta - \cos\xi}, \tag{29}$$

$$z = \frac{C\sinh\eta}{\cosh\eta - \cos\xi}. \tag{30}$$

C is a dimensionful constant which sets the scale of the coordinates and is chosen as $C = a_1\sinh\eta_0^+$. This choice fixes the $\eta = \eta_0^+$ coordinate surface to be coincident with the first hole. The coordinate surface defined as coincident with the second hole is labeled η_0^-. For given values of the configuration α and β defined in (27) and (28), $\eta_0^\pm$ take values of

$$\eta_0^+ = \ln\sqrt{\frac{\chi}{2} + \frac{1}{2}\sqrt{\chi^2 - 4}} \tag{31}$$

and

$$\eta_0^- = -\operatorname{arcsinh}(\alpha\sinh\eta_0^+), \tag{32}$$

where

$$\chi \equiv \beta^2 + \frac{1}{\beta^2}\left(1 + \frac{1}{\alpha^4}\right) - \frac{2}{\alpha^2}\left(1 + \frac{1}{\beta^2}\right). \tag{33}$$

The background metric takes the form

$$ds^2 = \frac{a_1^2 \sinh^2 \eta_0^+}{(\cosh\eta - \cos\xi)^2}(d\eta^2 + d\xi^2 + \sin^2\xi d\phi^2), \tag{34}$$

and the domain in which the Hamiltonian constraint must be solved is $\eta_0^- \le \eta \le \eta_0^+$, $0 \le \xi \le \pi$, and $0 \le \phi < 2\pi$.

If the elements of the boundary-value problem are expressed in terms of bispherical coordinates, the Laplacian takes the form

$$\begin{aligned}\bar{\nabla}^2\psi = {} & \frac{(\cosh\eta - \cos\xi)^3}{a_1^2 \sinh^2\eta_0^+} \\ & \times\left[\frac{\partial}{\partial\eta}\left(\frac{1}{\cosh\eta - \cos\xi}\frac{\partial\psi}{\partial\eta}\right)\right. \\ & \left.+\frac{1}{\sin\xi}\frac{\partial}{\partial\xi}\left(\frac{\sin\xi}{\cosh\eta - \cos\xi}\frac{\partial\psi}{\partial\xi}\right)\right] \\ & +\frac{1}{a_1^2\sinh^2\eta_0^+}\frac{(\cosh\eta - \cos\xi)^2}{\sin^2\xi}\frac{\partial^2\psi}{\partial\phi^2}.\end{aligned} \tag{35}$$

The boundary conditions (20) on the two inversion surfaces take the form

$$\left(-\frac{(\cosh\eta - \cos\xi)}{\sinh\eta}\frac{\partial\psi}{\partial\eta} + \frac{\psi}{2}\right)_{\eta=\eta_0^\pm} = 0. \tag{36}$$

Finally, asymptotic flatness is imposed by demanding the Dirichlet condition

$$\psi|_{(\eta=0,\xi=0)} = 1 \quad \text{for all } \phi. \tag{37}$$

The numerical approach used to solve the Hamiltonian constraint is that of finite differencing. In order to reduce the computational size of the problem, I will consider only axisymmetric configurations. This restriction means that the linear and angular momentum vectors for the two holes must be parallel to the line connecting the centers of the two holes. The method used to evaluate the extrinsic curvature for axisymmetric configurations is given in detail in Appendix A.

The restriction to axisymmetry introduces a new boundary condition which is imposed on the $\xi = 0$ and $\xi = \pi$ boundaries (except at $\eta = \xi = 0$). This condition is

$$\left.\frac{\partial\psi}{\partial\xi}\right|_{\xi=0,\pi} = 0. \tag{38}$$

This boundary condition can be used with L'Hôpital's rule to define an appropriate limiting form for the Laplacian on the axis of symmetry:

$$\begin{aligned}\lim_{\xi\to 0,\pi}\frac{1}{\sin\xi}\frac{\partial}{\partial\xi}\left(\frac{\sin\xi}{\cosh\eta - \cos\xi}\frac{\partial\psi}{\partial\xi}\right) \\ = 2\frac{\partial}{\partial\xi}\left(\frac{1}{\cosh\eta - \cos\xi}\frac{\partial\psi}{\partial\xi}\right).\end{aligned} \tag{39}$$

The discretization of the computational domain is not straightforward because it is necessary to impose a Dirichlet boundary condition at "infinity." In order to ensure that $\eta = \xi = 0$ is included in the discrete domain, I choose η to be a quadratic function of a new coordinate s and uniformly discretize s:

$$\begin{aligned}&\eta_i = \eta(s_i) = f * s_i^2 + g * s_i, \\ &s_i = i * h_s, \quad i = -\mathcal{S}^-, \ldots, 0, \ldots, \mathcal{S}^+, \\ &h_s = \frac{1}{\mathcal{S}^+ + \mathcal{S}^-}, \\ &f = (\mathcal{S}^+ + \mathcal{S}^-)\left(\frac{\eta_0^+}{\mathcal{S}^+} + \frac{\eta_0^-}{\mathcal{S}^-}\right), \\ &g = \frac{\mathcal{S}^-\eta_0^+}{\mathcal{S}^+} - \frac{\mathcal{S}^+\eta_0^-}{\mathcal{S}^-}.\end{aligned} \tag{40}$$

The integers $\mathcal{S}^+$ and $\mathcal{S}^-$ give the number of discrete points sampled above and below $\eta = 0$ and must be chosen so that η is a monotonically increasing function of s for $\eta_0^- \le \eta \le \eta_0^+$. The discretization of ξ is trivial and is given by

$$\xi_j = j * h_\xi, \quad \text{where} \quad j = 0, \ldots, \mathcal{J} \quad \text{and} \quad h_\xi = \frac{\pi}{\mathcal{J}}. \tag{41}$$

The Hamiltonian constraint and boundary conditions are differenced using vertex-centered, second-order, conservative finite differencing. The nonlinear difference equations are solved by Newton iterations on the linearized equations, and the linearized equations are solved by a "black-box" multigrid algorithm based on an approach developed by Dendy [22].

Given a solution, various quantities describing the physical content of the initial-data slice can be computed. The total energy content (ADM energy [17]) and dipole moment of the initial slice can be computed from the integrals (24) and (25). A more convenient form for evaluating these integrals numerically is obtained by using Gauss' law to transform each into the sum of a volume integral over the region exterior to the throats plus two surface integrals over the throats [7]. Two other quantities of interest are the physical surface area of the throats and the proper separation of the throats. The physical surface area for each throat is computed from

$$A_{MS} = \oint_{r=a_\alpha} \psi^4 d^2\bar{S}. \tag{42}$$

The proper separation of the two holes is given by an integral of the physical metric along the line connecting the two holes. In terms of bispherical coordinates, this is given by

$$L = a_1 \sinh\eta_0^+ \int_{\eta_0^-}^{\eta_0^+} \frac{\psi^2_{(\xi=\pi)}}{\cosh\eta + 1} d\eta. \tag{43}$$

There are two useful tests which can be performed to check the validity and accuracy of the code's solutions. The first test makes use of Misner's analytic solution in the case of time symmetry. The code has been run for $\alpha = 1$ and $\beta = 3, 4, \ldots, 12$ with grid resolutions of (80×80), (160×160), and (320×320) for each configuration. Using results from the three solutions, physical quantities computed on the slice can be Richardson extrapolated to the continuum limit and compared with the values from Misner's analytic solution. In the case of the total

TABLE I. Total energy E/a_1 and masses $M^{\pm}/a_1$ for two holes which are very far apart with one hole much larger than the other and having linear momentum P, compared with the total energy E/a and mass M/a of a single hole with the same momentum. The extrinsic curvatures obey the isometry condition with the plus sign. ($\alpha = 20, \beta = 50.$)

P/a_1	E/a_1	M^+/a_1	M^-/a_1	$(E-M^-)/a_1$	E/a	M/a
0.0	2.102	2.000	0.104	1.998	2.000	2.000
1.0	2.448	2.112	0.104	2.344	2.347	2.113
2.5	3.689	2.469	0.107	3.582	3.589	2.470
5.0	6.235	3.066	0.112	6.123	6.132	3.069
7.5	8.926	3.586	0.116	8.810	8.815	3.589
10.0	11.67	4.045	0.121	11.55	11.54	4.049
12.5	14.43	4.458	0.126	14.30	14.29	4.463
15.0	17.22	4.838	0.130	17.09	17.04	4.843
17.5	20.01	5.190	0.134	19.88	19.81	5.195

ADM energy of the slice, the relative error between the analytic and the Richardson-extrapolated values ranged from 0.003% at $\beta = 3$ to 0.01% at $\beta = 12$. Similar results were found for $\alpha \neq 1$.

This set of tests, unfortunately, only examines the code in the time-symmetric regime where the Hamiltonian constraint is linear. It does not test the nonlinear aspects of the constraint solver, the computation of the extrinsic curvature, or the volume integrals for E and d_i. While there are no known analytic solutions to the full, nonlinear problem for multiple holes, many researchers have computed accurate numerical solutions for the case of a single, inversion-symmetric hole. By letting α and β be very large, the resulting two-hole configuration is essentially that of one hole perturbed by a small, distant hole. If the two holes are far enough apart, then the binding energy is negligible compared to the total energy. Subtracting the mass of the small, perturbing hole M^-/a_1 from the total energy E/a_1 gives an energy for the remaining hole which has linear or angular momentum. Table I compares the results from one-hole solutions against solutions of analogous configurations of the two-hole code in the case that the hole has linear momentum. The effective scaled energy $(E-M^-)/a_1$ associated with the large hole in the bispherical code should be compared with the scaled energy E/a from the one-hole computations. The scaled mass of the large hole M^+/a_1 should be compared to the scaled mass M/a from the one-hole computations. Though all cases are not displayed in tabular form, configurations in which the hole had angular momentum and where the hole had linear momentum generated from an extrinsic curvature satisfying isometry condition (9) with both signs were explored. In all cases, the relative error between results from the one- and two-hole codes was less than 0.5%.

VI. THE ČADEŽ SCHEME

The second scheme for solving the Hamiltonian constraint is based upon the use of Čadež coordinates. As mentioned before, the Čadež coordinate system is constructed numerically and is described in Appendix C. The two Čadež coordinates η and ξ are based in cylindrical coordinates. $\eta(\rho, z)$ is a radial-like coordinate and $\xi(\rho, z)$ is an angular coordinate. The coordinate system is logically composed of three regions (see Fig. 1):

$$\text{region } 1 \equiv \begin{cases} \eta^+ \leq \eta < \eta_s, \\ 0 \leq \xi \leq \xi_s, \end{cases} \tag{44a}$$

$$\text{region } 2 \equiv \begin{cases} \eta^- \leq \eta < \eta_s, \\ \xi_s \leq \xi \leq \pi, \end{cases} \tag{44b}$$

$$\text{region } 3 \equiv \begin{cases} \eta_s \leq \eta < \infty, \\ 0 \leq \xi \leq \pi. \end{cases} \tag{44c}$$

Region 1 surrounds the first hole out to the singular point at (η_s, ξ_s). Region 2 surrounds the second hole out to the singular point, and region 3 surrounds both holes outside of the singular point.

The background metric takes the form

$$ds^2 = \frac{a_1^2}{\eta_{,\rho}^2 + \eta_{,z}^2}(d\eta^2 + d\xi^2) + a_1^2\rho^2 d\phi^2, \tag{45}$$

where ρ and z are dimensionless cylindrical coordinates scaled relative to a_1. The Laplacian can be written as

$$\bar{\nabla}^2\psi = \frac{\eta_{,\rho}^2 + \eta_{,z}^2}{a_1^2\rho}\left[\frac{\partial}{\partial\eta}\left(\rho\frac{\partial\psi}{\partial\eta}\right) + \frac{\partial}{\partial\xi}\left(\rho\frac{\partial\psi}{\partial\xi}\right)\right] + \frac{1}{a_1^2\rho^2}\frac{\partial^2\psi}{\partial\phi^2}, \tag{46}$$

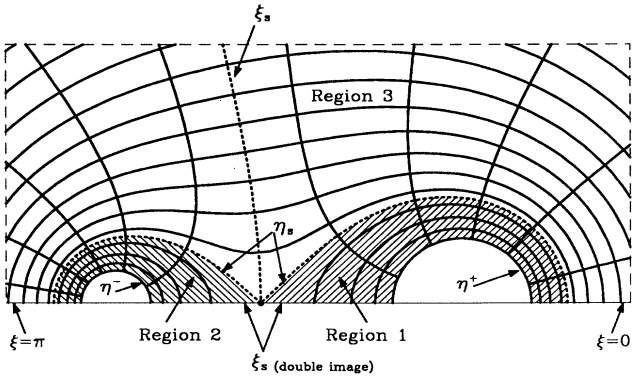

FIG. 1. Čadež coordinates near the two holes showing the *three* region nature of the coordinate system. (η_s, ξ_s) is the singular point in the coordinate system. $\eta^{\pm}$ are the constant coordinate surfaces coincident with the minimal surfaces.

which is an appropriate form for conservative differencing. The boundary conditions on the two inversion surfaces take the forms

$$\left(\sqrt{\eta_{,\rho}^2+\eta_{,z}^2}\frac{\partial\psi}{\partial\eta}+\frac{\psi}{2}\right)_{\eta=\eta^+}=0 \tag{47}$$

and

$$\left(\sqrt{\eta_{,\rho}^2+\eta_{,z}^2}\frac{\partial\psi}{\partial\eta}+\frac{\alpha\psi}{2}\right)_{\eta=\eta^-}=0. \tag{48}$$

Finally, asymptotic flatness is imposed on a boundary at finite radius, ($\eta=\eta_f$), via the approximate boundary condition (26) which takes the form

$$\begin{aligned}\frac{\partial\psi}{\partial\eta}=&\frac{z\eta_{,\rho}-\rho\eta_{,z}}{z\eta_{,z}+\rho\eta_{,\rho}}\frac{\partial\psi}{\partial\xi}+\frac{1-\psi}{z\eta_{,z}+\rho\eta_{,\rho}}\\&-\frac{(d_z/a_1^2)z}{2(z\eta_{,z}+\rho\eta_{,\rho})(\rho^2+z^2)^{3/2}}\\&-\frac{9}{32}\frac{[(P_1/a_1)+(P_2/a_1)]^2(z^2-\rho^2)}{(z\eta_{,z}+\rho\eta_{,\rho})(\rho^2+z^2)^2}\end{aligned} \tag{49}$$

in the case of axisymmetric configurations. d_z/a_1^2 is the dimensionless z component of the dipole moment and $P_{1,2}/a_1$ are the dimensionless z components of the linear momenta on the two holes.

The numerical approach to solve the Hamiltonian constraint will again be to use finite differences. Also, as in the bispherical case, only axisymmetric configurations will be treated. The method used to evaluate the extrinsic curvature for the bispherical scheme (and described in Appendix A) is also used in the Čadež scheme.

Axisymmetry again introduces a new boundary condition on the z axis. The condition is

$$\frac{\partial\psi}{\partial\xi}=0,\quad \text{for } \xi=\begin{cases}0,\pi,\\ \xi_s \text{ for } \eta\le\eta_s.\end{cases} \tag{50}$$

The discretization of the computational domain, and thus the differencing of the Hamiltonian constraint, is complicated by the presence of the coordinate singularity at (η_s,ξ_s). It was, in fact, improper handling of the discretization at this point which foiled an earlier attempt to find inversion-symmetric solutions to the two-hole Hamiltonian constraint [14]. There are at least two good approaches for handling the discretization. One approach is to guarantee that a grid point is placed exactly on the singular point and difference the Laplacian at the singular point by treating the neighboring grid points as being irregularly spaced in cylindrical coordinates [21]. A second approach is to guarantee that the singular point is zone centered and thus never lies on a grid point [23]. The differencing of the Hamiltonian constraint is simpler and better behaved in the latter case and is the method described below.

The "radial" coordinate η is discretized as

$$\eta_i=(i-\tfrac{1}{2})h_\eta+\eta_s, \tag{51a}$$

$$i=\begin{cases}-\mathcal{I}^+,\ldots,0 & \text{region 1,}\\ -\mathcal{I}^-,\ldots,0 & \text{region 2,}\\ 1,\ldots,\mathcal{I} & \text{region 3,}\end{cases} \tag{51b}$$

and

$$h_\eta=\frac{\eta_f-\eta_s}{\mathcal{I}-\frac{1}{2}}=\frac{\eta_s-\eta^-}{\mathcal{I}^-+\frac{1}{2}}=\frac{\eta_s-\eta^+}{\mathcal{I}^+-\frac{1}{2}}. \tag{51c}$$

The same discretization length h_η is possible in both regions 1 and 2 even when the holes are of unequal size because there is freedom in the definition of the Čadež coordinates to place the singular point anywhere along the z axis between the holes. The discretization of the ξ coordinate is performed in a fashion similar to the discretization of the bispherical-η coordinate:

$$\begin{aligned}&\xi_j=\xi(s_j)=\bar f * s_j^2+\bar g * s_j,\\&s_j=(j-\tfrac{1}{2})h_s,\quad j=1,\ldots,\mathcal{S}^+,\ldots,\mathcal{S}^++\mathcal{S}^-,\\&h_s=\frac{1}{\mathcal{S}^++\mathcal{S}^-},\\&\bar f=\frac{(\mathcal{S}^++\mathcal{S}^-)\pi}{\mathcal{S}^-}-\frac{(\mathcal{S}^++\mathcal{S}^-)^2\xi_s}{\mathcal{S}^+\mathcal{S}^-},\\&\bar g=\frac{(\mathcal{S}^++\mathcal{S}^-)^2\xi_s}{\mathcal{S}^+\mathcal{S}^-}-\frac{\mathcal{S}^+\pi}{\mathcal{S}^-}.\end{aligned} \tag{52}$$

The integers $\mathcal{S}^+$ and $\mathcal{S}^-$ give the number of discrete points above and below ξ_s and must be chosen so that ξ is a monotonically increasing function of s for $0\le\xi\le\pi$.

The Hamiltonian constraint and boundary conditions are differenced using vertex-centered, second-order, conservative finite differencing as in the case of the bispherical scheme, and the nonlinear difference equations

TABLE II. ADM energy of time-symmetric solutions of the Hamiltonian constraint at three different mesh resolutions (in Čadež coordinates), Richardson extrapolated and compared with the analytic solution for the ADM energy. β indicates the separation of the two holes. The outer boundary is at $\sim 200a_1$.

β	E/a_1 ($\sim 64\times 32$)	E/a_1 ($\sim 128\times 64$)	E/a_1 ($\sim 256\times 128$)	E/a_1 (extrap.)	E/a_1 (analytic)	Relative error
4	5.4419	5.3789	5.3674	5.3636	5.3642	−0.011%
5	5.0244	5.0125	5.0109	5.0103	5.0106	−0.006%
6	4.8057	4.8040	4.8043	4.8045	4.8046	−0.002%
7	4.6664	4.6677	4.6686	4.6689	4.6690	−0.002%
8	4.5691	4.5714	4.5723	4.5726	4.5727	−0.002%
9	4.4971	4.4995	4.5004	4.5007	4.5008	−0.002%
10	4.4416	4.4438	4.4446	4.4449	4.4449	< 0.001%
11	4.3975	4.3994	4.4001	4.4003	4.4003	< 0.001%
12	4.3587	4.3623	4.3635	4.3638	4.3639	−0.002%

are solved iteratively via Newton's method. The same "black-box" multigrid solver used for the bispherical scheme was used with the Čadež scheme. As in the bispherical case, the total ADM energy and dipole moment are computed for each solution along with the areas of the minimal surfaces and the proper separation between the minimal surfaces.

As a first test of the accuracy of the Čadež code, Table II lists the total ADM energy for a set of runs where $\alpha = 1$ and $\beta = 4$–12. For each value of β, the code was run at three resolutions and the results are Richardson extrapolated to the continuum limit. Because of the constraints on the radial discretization imposed by the singularity in Čadež coordinates, $\beta = 3$ is not included in this table. Also, the same constraint forces the radial discretization of each value of β to be different although each is chosen to be nearly 64 zones on the coarsest grid when the outer boundary is at $\sim 200a_1$.

VII. SOLUTIONS FOR BOOSTED AND SPINNING HOLES

Using the two codes described above, an enormous parameter space exists in which solutions can be explored. If we consider axisymmetric solutions of the constraints for which the conformal factor obeys isometry condition (9) with a minus sign, then there is a six-dimensional parameter space (α, β, P_1, P_2, S_1, and S_2) to be explored. For solutions obeying isometry condition (9) with a plus sign, the parameter space is four dimensional (because there can be no spin). Both of these parameter spaces are far too large to be explored effectively by the numerical techniques described above. In this section, I will consider the following reduced parameter spaces.

Six two-dimensional parameter spaces can be constructed by assuming that the two holes are of equal size and have linear or angular momenta of equal magnitude. If we consider solutions of the constraint equations for which the extrinsic curvature satisfies isometry condition (9) with a plus sign, then we find two configurations. The first has the linear momentum vectors aligned antiparallel to each other so that there is no net momentum at infinity, and the second has the linear momentum vectors aligned parallel to each other. The third and fourth configurations are identical to the first two except that the extrinsic curvature satisfies the isometry condition with the minus sign. The final pair of configurations represent holes with angular momenta aligned either antiparallel or parallel. For clarity and brevity in the discussion below, I will refer to these configurations, respectively, as cases 1–6. For each of these cases, there are two remaining parameters to be explored. The separation between the two holes can be varied, and this quantity is roughly parametrized by the "conformal separation" parameter β. The second parameter to be varied in each initial-data set is the magnitude of the linear momentum P or angular momentum S for each of the holes.

All six configurations have been explored extensively, solving identical configurations with both the bispherical and Čadež codes to allow for comparison. For the bispherical code, each point in the parameter space was solved at three different grid resolutions as described for the time-symmetric test cases in Sec. V. Solutions from the Čadež code were also found at three different grid resolutions as described for the time-symmetric test cases in Table II. For the case of $\beta = 3$, the Čadež code was only run at two resolutions, (298 × 148) and (496 × 296). For each point in the parameter space, the values for the total ADM energy, the area of the minimal surfaces, and the proper separation of the holes were Richardson extrapolated to the continuum limit and the results from the bispherical and Čadež codes were compared. For the total ADM energy, agreement between the bispherical- and Čadež-extrapolated results was typically at the 0.01% level. The worst agreement occurred when there was a large net linear or angular momentum for the configuration. In these cases, the outer boundary in the Čadež code was as close at $4M_T$ (where M_T is the total mass of the system). In these cases, the error was as high as 2.5%, but this can be lowered by increasing the radius of the outer boundary. Agreement between the bispherical and Čadež codes for the minimal surface area and proper separation were typically 0.02%. For small values of β, the error in the proper separation was as high as 0.4%, due to the relatively small number of grid points that the Čadež coordinate scheme places between the holes. In the remainder of this section, I will examine the content of the initial-data sets which have been constructed for the six cases described above.

In examining and comparing physical quantities associated with these initial-data sets, it will be necessary to find some kind of *natural* scaling. The proper separation of the two holes, for example, is less meaningful than the separation-to-mass ratio. The question, of course, is how to scale the quantities in such a way as to clarify the problem. It is perhaps most natural to scale all of the physical quantities in terms of the "mass" of one of the holes. The mass of each hole, while not uniquely defined, will be taken to be defined similarly to the Christodoulou formula [24]

$$M^2 = M_{\rm ir}^2 + \frac{S^2}{4M_{\rm ir}^2}. \tag{53}$$

The irreducible mass $M_{\rm ir}$ of one of the holes cannot be defined solely from the information on a single slice of the space-time. In fact, if there is an event horizon encompassing both holes, then the irreducible mass of an individual hole is not even defined. However, we can determine the area (and thus the mass $M = \sqrt{A/16\pi}$) of the *apparent horizon* from information in the initial-data slice. Even when a horizon encompasses both holes, there will be a trapped surface (though not an apparent horizon) associated with the individual holes. The mass of a hole will, thus, be taken to be given by the Christodoulou formula (53) with the irreducible mass replaced by the mass of the apparent horizon (or trapped surface).

In general, it is necessary to implement a trapped-surface locator in order to determine the area of the apparent horizon associated with each hole. This has not yet been attempted in the two codes which compute the

initial data. Fortunately, it is shown in Appendix D that when the extrinsic curvature satisfies isometry condition (9) with a minus sign (cases 3–6), the minimal surface is a trapped surface. Thus, the mass of the apparent horizon equals the mass of the minimal surface which *is* known. For cases 1 and 2 in which the location of the trapped surface for each hole is not known, the mass of the minimal surface has been used as a lower limit on the mass of the apparent horizon.

Figures 2–5 below display the naturally scaled physical quantities which correspond, respectively, to cases 3–6. Plots corresponding to cases 1 and 2 are not shown since they are qualitatively the same as those for cases 3 and 4. Each figure displays four characterizing physical quantities as a function of the naturally scaled linear or angular momentum on *one* of the holes and evaluated at six different values of the separation parameter $\beta = 3, 4, 6, 8, 10, 12$. Plotted in Figs. 2(a)–5(a) is the scaled total ADM energy E/M of the slice. If we consider the case of two Kerr holes infinitely far apart, then E/M for the system will be *two* regardless of the magnitude of the angular momenta on the holes. Plot (b) in each figure displays the scaled proper separation L/M of the two holes. If we assume that the two holes will eventually coalesce into a single boosted Schwarzschild or Kerr hole, then we can use Hawking's area theorem [25] to determine a lower limit on the final mass of the resulting black hole. If S_1 and S_2 are the signed magnitudes of the spins on the two holes, each having an apparent horizon of mass $M_{\rm AH}$ on the initial slice, then the final mass of the hole M_f must be

$$M_f > M_{\rm AH}\sqrt{2 + \frac{1}{8}\left(\frac{S_1 + S_2}{M_{\rm AH}^2}\right)^2}. \tag{54}$$

If P_1 and P_2 are the signed magnitudes of the linear momenta of the two holes, then an upper limit on the amount of energy which can possibly be radiated from the system in the form of gravitational radiation is

$$E_{\rm rad} < \sqrt{E^2 - (P_1 + P_2)^2} - M_{\rm AH}\sqrt{2 + \frac{1}{8}\left(\frac{S_1 + S_2}{M_{AH}^2}\right)^2}. \tag{55}$$

The maximum possible radiation content of the slice, scaled to the mass of one of the holes, is displayed in plot (c) of each figure. Finally, plot (d) in each figure displays the maximum radiation efficiency of each slice

$$\text{efficiency} < \frac{E_{\rm rad}}{\sqrt{E^2 - (P_1 + P_2)^2}}. \tag{56}$$

Consider first Fig. 2 which represents two holes with antiparallel linear momentum vectors. This can represent either two holes headed directly toward *or* away from each other. The energy, mass, and separation are identical in either instance. As mentioned above, if the two holes are at rest infinitely far apart, then E/M should be *two*. Thus, any configuration with $E/M < 2$ should be gravitationally bound. The first thing that is noticed in Fig. 2(a) is the increasing effect of negative binding energy as the separation parameter β is decreased. We also see that if the two holes are far enough apart and have large enough momenta, then it seems energetically feasible (if the momenta are directed away from each other) for the two holes to be unbound. Examining Fig. 2(b), we find that the conformal separation param-

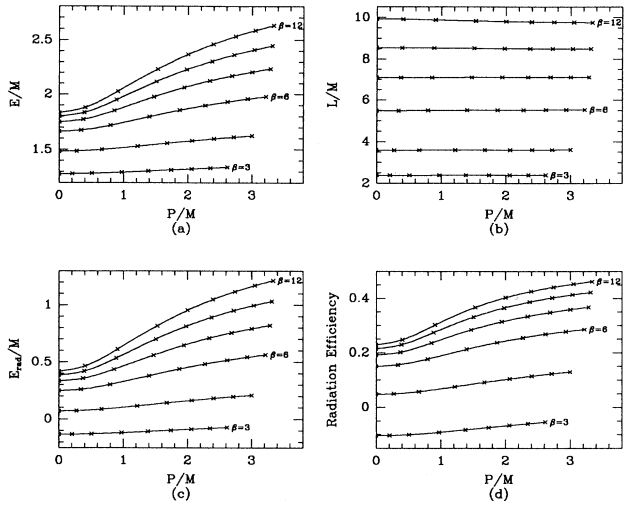

FIG. 2. (a) Total energy, (b) separation, (c) maximum radiation energy, and (d) maximum radiation efficiency for two equal-sized holes with axisymmetric linear momenta P aligned antiparallel to each other and generated from an inversion-symmetric extrinsic curvature obeying the isometry condition with a minus sign. The conformal separation parameter is fixed along each sequence with $\beta = 3, 4, 6, 8, 10, 12$ increasing from bottom to top.

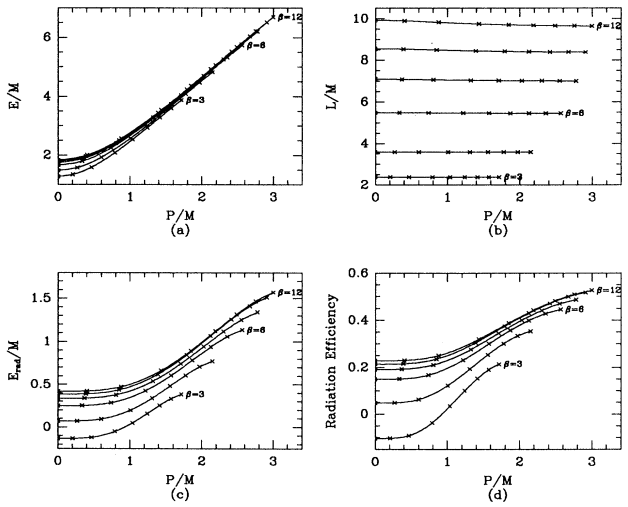

FIG. 3. (a) Total energy, (b) separation, (c) maximum radiation energy, and (d) maximum radiation efficiency for two equal-sized holes with axisymmetric linear momenta P aligned parallel to each other and generated from an inversion-symmetric extrinsic curvature obeying the isometry condition with a minus sign. The conformal separation parameter is fixed along each sequence with $\beta = 3, 4, 6, 8, 10, 12$ increasing from bottom to top.

eter is strongly correlated with the physical separation-to-mass ratio L/M. This is somewhat unexpected given the nonlinearity of Einstein's equations.

If the two holes coalesce, then Fig. 2(c) shows the scaled maximum amount of energy which can be released via gravitational radiation. As expected, $E_{\rm rad}/M$ increases as both separation and momentum increase. An unusual feature is seen for $\beta = 3$. In this case, the energy available for radiation is negative. This behavior must be due to the inappropriate application of Eq. (55). At this point, a horizon must have formed surrounding the two holes. This is confirmed by the numerical work of Čadež [2], where he has found that an apparent horizon will surround two time-symmetric, inversion-symmetric holes if $\beta \leq 4.16$.

Figure 3 represents the case of two holes with parallel linear momenta. Examining the scaled total energy in Fig. 3(a) shows the gross behavior of a single boosted particle, although at lower values of the momentum the lowering of the total energy due to increased binding energy as the holes are brought closer is clearly visible. Figure 3(b) shows that the L/M ratio is again fairly insensitive to P/M. Figures 3(c) and 3(d) show little new information about the radiative potential of the initial slice beyond that already seen for a single boosted hole [12]. The differences result primarily from the effects of binding energy.

The most interesting of the configurations are cases 5 and 6, which involve two holes with antiparallel and parallel angular momentum vectors and the behaviors of which are displayed, respectively, in Figs. 4 and 5. The behaviors of the scaled total energy displayed in Figs. 4(a) and 5(a) are surprising and unintuitive. While they clearly show the effects of binding energy as the holes are brought closer together, they also indicate that the total energy-to-mass ratio decreases as the angular momenta increase, with the decrease being most dramatic when the spins are antiparallel.

Examining the L/M ratio in Figs. 4(b) and 5(b) shows that it is much more strongly affected by the spin of the holes than by their linear momenta. This fact complicates the interpretation of the total energy of the slice seen in Figs. 4(a) and 5(a) because the constant β sequences no longer have nearly constant values for the separation-to-mass ratio. Since the holes are getting closer for constant β as the angular momenta are increased, they necessarily have greater binding energy and the decrease in E/M must be due, in part, to this effect. However, rough interpolation along lines of constant L/M clearly shows that the decrease in separation is not the dominant contribution to the decrease in E/M at large values of angular momentum. It is possible that the Christodoulou mass is not the correct quantity with which to scale the total energy and separation. On the other hand, its use in the scaling of the angular momentum does have the correct limiting behavior as the angular momentum is increased. That is, S/M^2 appears to be asymptotic to *one*, which is the "Kerr" limit. The "odd" behavior of the scaled energy is more likely due to a combination of the behavior of L/M at low values of momentum and the appearance of a horizon surrounding the two holes at large values of momentum. A more thorough understanding of this behavior will likely require a search for the apparent horizons in these data sets.

Moving on to examine the radiative potential of the slices, consider first Figs. 4(c) and 4(d) which represent

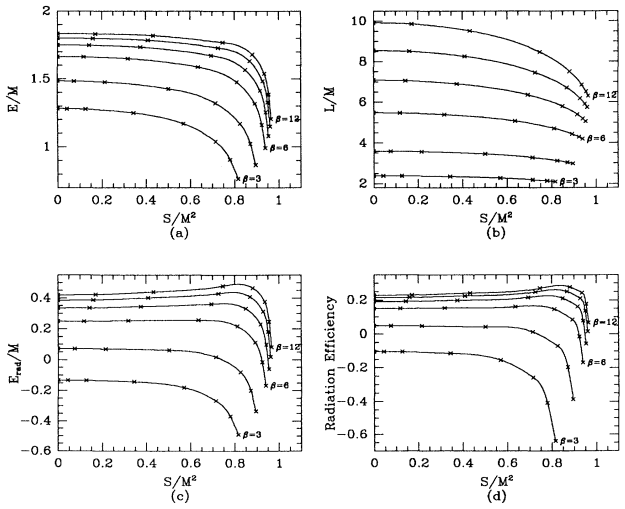

FIG. 4. (a) Total energy, (b) separation, (c) maximum radiation energy, and (d) maximum radiation efficiency for two equal-sized holes with axisymmetric angular momenta S aligned antiparallel to each other and generated from an inversion-symmetric extrinsic curvature obeying the isometry condition with a minus sign. The conformal separation parameter is fixed along each sequence with $\beta = 3, 4, 6, 8, 10, 12$ increasing from bottom to top.

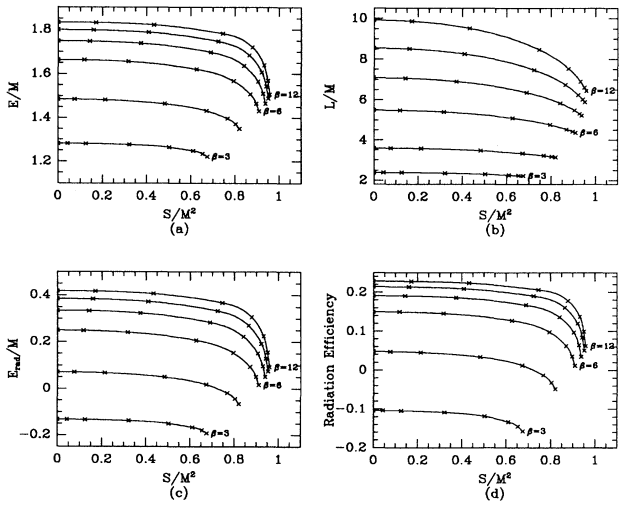

FIG. 5. (a) Total energy, (b) separation, (c) maximum radiation energy, and (d) maximum radiation efficiency for two equal-sized holes with axisymmetric angular momenta S aligned parallel to each other and generated from an inversion-symmetric extrinsic curvature obeying the isometry condition with a minus sign. The conformal separation parameter is fixed along each sequence with $\beta = 3, 4, 6, 8, 10, 12$ increasing from bottom to top.

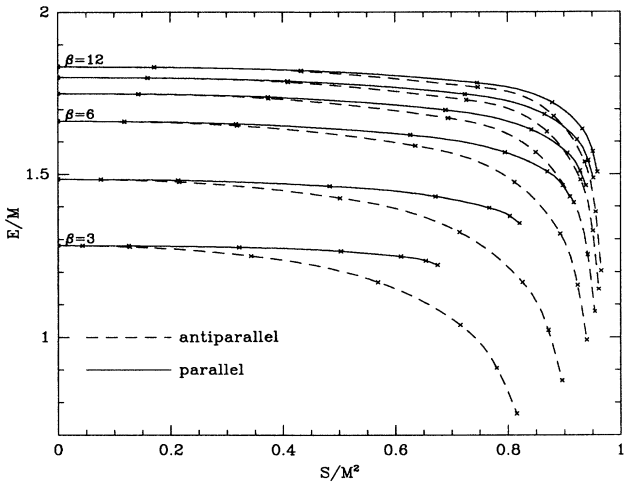

FIG. 6. Comparison of the scaled total energy for two equal-sized holes with axisymmetric angular momenta S aligned antiparallel (dashed lines) and parallel (solid lines) to each other showing the spin-spin interaction. The conformal separation parameter is fixed along each sequence with $\beta = 3, 4, 6, 8, 10, 12$ increasing from bottom to top.

the case of two holes with antiparallel spins. We see that the amount of energy which is potentially available for radiation does increase initially as the angular momentum is increased. However, after a certain point, the available energy rapidly diminishes with increased angular momentum. These effects are seen not only in $E_{\rm rad}/M$ but also in the efficiency which is a ratio that is independent of the scaling parameter. This indicates that the drop in energy cannot be due to the choice in scaling parameter and is either a physical effect or is associated with the presence of an encompassing horizon. Examining Figs. 5(c) and 5(d), we find that the amount of energy which is potentially available for radiation and the radiation efficiency both decrease continuously as the angular momentum is increased.

Finally, one more physical aspect of the two-hole interaction can be seen by examining these two-hole initial-data sets. The gravitational spin-spin interaction has been investigated by Wald [26] for the case of a spinning test particle in the exterior field of an arbitrary, stationary, rotating source. The orientation dependence of this interaction can be seen by comparing the scaled energy-versus-momentum sequences from cases 5 and 6. Figure 6 presents an overlay of Figs. 4(a) and 5(a). It is apparent that the total energy of the system along constant β sequences is lower when the spins are antialigned than when aligned. This implies that the spin-spin interaction is attractive when the spins are antialigned and repulsive when aligned, as was found by Wald. This conclusion is somewhat clouded by the fact that constant β sequences do not represent sequences with constant L/M; however, the L/M curves for constant β are nearly identical for both the parallel and antiparallel spin scenarios so the comparison is valid. In addition to observing the spin-orientation dependence, a qualitative separation dependence is also apparent from Fig. 6. We see that the magnitude of the spin-spin force decreases as the separation between the holes increases from the fact that the difference in the energy levels for the aligned and antialigned cases decreases with increasing separation.

VIII. CONCLUSION

This paper has shown that highly accurate, complete, axisymmetric initial-data sets representing black-hole collisions can be constructed following the conformal-imaging formalism. Because a completely general, three-dimensional method for evaluating the inversion-symmetric background extrinsic curvature has been devised, future efforts at constructing general three-dimensional initial-data sets need only confront the numerical solution of the Hamiltonian constraint. The numerical difficulties and computational resources required to construct such solutions are considerable, but the problem should be tractable with current facilities.

A preliminary analysis of the data sets constructed in this paper has shown that the black holes present in the initial-data slices exhibit the general properties which we expect to find in two-hole configurations (binding energy, spin-spin interaction, etc.). The analysis presented herein is, however, incomplete and a more thorough investigation is under way [16] which includes a search for apparent horizons and an investigation of the initial radiation content of the data sets.

ACKNOWLEDGMENTS

I gratefully acknowledge many useful discussions with J. W. York, Jr., C. R. Evans, T. Piran, A. Abrahams, and D. W. Hobill. This work was supported in part by the National Science Foundation under Grant Nos. PHY-8407492, PHY-8908741, PHY-9001645, and PHY-9007834. Computations were performed primarily at the Cornell National Supercomputer Facility which is supported in part by the National Science Foundation, IBM Corporation, New York State, and the Cornell Research Institute. Computations were also performed at the North Carolina Supercomputing Center.

APPENDIX A: NUMERICAL EVALUATION OF THE INVERSION-SYMMETRIC EXTRINSIC CURVATURE

For the case of two black holes, the components of the inversion-symmetric extrinsic curvature can be expressed, as in Eq. (19), in terms of an infinite series of recursively defined quantities. In the first part of this appendix, I will formally define these recurrence relations. Following this, I will show, in detail, how these relations (and the components of the extrinsic curvature) are evaluated in cylindrical coordinates in the case of axisymmetry.

Let J_1^i and J_2^i be the isometry maps which identify points in the two sheets through, respectively, the first and second hole. Further, let $(J_1)^i_j = \partial J_1^i/\partial x^j$ and $(J_2)^i_j = \partial J_2^i/\partial x^j$ be the Jacobians of these maps. Finally,

assume that we wish to evaluate the inversion-symmetric extrinsic curvature at some point x^i.

The two "imaged" position vectors $(x_1^n)^i$ and $(x_2^n)^i$ are recursively defined by

$$(x_1^n)^i \equiv \begin{cases} J_{1(x_1^{n-1})}^i & \text{for } n \text{ odd}, \\ J_{2(x_1^{n-1})}^i & \text{for } n \text{ even}, \\ x^i & \text{for } n = 0, \end{cases} \tag{A1}$$

$$(x_2^n)^i \equiv \begin{cases} J_{2(x_2^{n-1})}^i & \text{for } n \text{ odd}, \\ J_{1(x_2^{n-1})}^i & \text{for } n \text{ even}, \\ x^i & \text{for } n = 0. \end{cases} \tag{A2}$$

The two "imaged" transformation matrices $(M_1^n)_j^i$ and $(M_2^n)_j^i$ are recursively defined by

$$(M_1^n)_j^i \equiv \begin{cases} (M_1^{n-1})_\ell^i (J_1)_{j(x_1^{n-1})}^\ell & \text{for } n \text{ odd}, \\ (M_1^{n-1})_\ell^i (J_2)_{j(x_1^{n-1})}^\ell & \text{for } n \text{ even}, \\ \delta_j^i & \text{for } n = 0, \end{cases} \tag{A3}$$

$$(M_2^n)_j^i \equiv \begin{cases} (M_2^{n-1})_\ell^i (J_2)_{j(x_2^{n-1})}^\ell & \text{for } n \text{ odd}, \\ (M_2^{n-1})_\ell^i (J_1)_{j(x_2^{n-1})}^\ell & \text{for } n \text{ even}, \\ \delta_j^i & \text{for } n = 0. \end{cases} \tag{A4}$$

Finally, the two "imaged" scale factors F_1^n and F_2^n are recursively defined by

$$F_1^n \equiv \begin{cases} F_1^{n-1} \left(\frac{a_1}{r_1}\right)^2_{(x_1^{n-1})} & \text{for } n \text{ odd}, \\ F_1^{n-1} \left(\frac{a_2}{r_2}\right)^2_{(x_1^{n-1})} & \text{for } n \text{ even}, \\ 1 \text{ for } n = 0, \end{cases} \tag{A5}$$

$$F_2^n \equiv \begin{cases} F_2^{n-1} \left(\frac{a_2}{r_2}\right)^2_{(x_2^{n-1})} & \text{for } n \text{ odd}, \\ F_2^{n-1} \left(\frac{a_1}{r_1}\right)^2_{(x_2^{n-1})} & \text{for } n \text{ even} \\ 1 \text{ for } n = 0. \end{cases} \tag{A6}$$

Consider now the case of axisymmetry. I will use cylindrical coordinates $[\rho \quad \phi \quad z]$, and make use of the configuration parameters α and β defined in (27) and (28). For the centers of the holes, I will define

$$C_1^i = [0 \quad 0 \quad a_1\zeta_1] \quad \text{and} \quad C_2^i = [0 \quad 0 \quad a_1\zeta_2]. \tag{A7}$$

The physical, unscaled linear and angular momentum vectors are

$$P_1^i = [0 \quad 0 \quad P_1] \quad \text{and} \quad P_2^i = [0 \quad 0 \quad P_2] \tag{A8}$$

and

$$S_1^i = [0 \quad 0 \quad S_1] \quad \text{and} \quad S_2^i = [0 \quad 0 \quad S_2]. \tag{A9}$$

The cylindrical coordinate components of $\hat{A}_{ij}$, defined in Eq. (18), can be written in dimensionless form as

$$\frac{\hat{A}_{\rho\rho}}{a_1} = -\frac{3}{2}\left(\frac{\left(\frac{P_1}{a_1}\right)(z-\zeta_1)^3}{[\rho^2+(z-\zeta_1)^2]^{5/2}} + \frac{\left(\frac{P_2}{a_1}\right)(z-\zeta_2)^3}{[\rho^2+(z-\zeta_2)^2]^{5/2}}\right), \tag{A10}$$

$$\frac{\hat{A}_{\phi\phi}}{a_1} = -\frac{3}{2}\rho^2\left(\frac{\left(\frac{P_1}{a_1}\right)(z-\zeta_1)}{[\rho^2+(z-\zeta_1)^2]^{3/2}} + \frac{\left(\frac{P_2}{a_1}\right)(z-\zeta_2)}{[\rho^2+(z-\zeta_2)^2]^{3/2}}\right), \tag{A11}$$

$$\frac{\hat{A}_{zz}}{a_1} = \frac{3}{2}\left(\frac{\left(\frac{P_1}{a_1}\right)(z-\zeta_1)\left[\rho^2+2(z-\zeta_1)^2\right]}{[\rho^2+(z-\zeta_1)^2]^{5/2}} + \frac{\left(\frac{P_2}{a_1}\right)(z-\zeta_2)\left[\rho^2+2(z-\zeta_2)^2\right]}{[\rho^2+(z-\zeta_2)^2]^{5/2}}\right), \tag{A12}$$

$$\frac{\hat{A}_{\rho z}}{a_1} = \frac{3}{2}\rho\left(\frac{\left(\frac{P_1}{a_1}\right)\left[\rho^2+2(z-\zeta_1)^2\right]}{[\rho^2+(z-\zeta_1)^2]^{5/2}} + \frac{\left(\frac{P_2}{a_1}\right)\left[\rho^2+2(z-\zeta_2)^2\right]}{[\rho^2+(z-\zeta_2)^2]^{5/2}}\right), \tag{A13}$$

$$\frac{\hat{A}_{\rho\phi}}{a_1} = \frac{3}{2}\rho^3\left(\frac{\left(\frac{S_1}{a_1^2}\right)}{[\rho^2+(z-\zeta_1)^2]^{5/2}} + \frac{\left(\frac{S_2}{a_1^2}\right)}{[\rho^2+(z-\zeta_2)^2]^{5/2}}\right), \tag{A14}$$

$$\frac{\hat{A}_{\phi z}}{a_1} = \frac{3}{2}\rho^2\left(\frac{\left(\frac{S_1}{a_1^2}\right)(z-\zeta_1)}{[\rho^2+(z-\zeta_1)^2]^{5/2}} + \frac{\left(\frac{S_2}{a_1^2}\right)(z-\zeta_2)}{[\rho^2+(z-\zeta_2)^2]^{5/2}}\right). \tag{A15}$$

The isometry maps J_1^i and J_2^i can be written in terms of dimensionless cylindrical coordinates as

$$J_1^i = \left(\frac{\rho}{\rho^2+(z-\zeta_1)^2} \quad \phi \quad \frac{z-\zeta_1}{\rho^2+(z-\zeta_1)^2}+\zeta_1\right), \tag{A16}$$

$$J_2^i = \left(\frac{\alpha^{-2}\rho}{\rho^2+(z-\zeta_2)^2} \quad \phi \quad \frac{\alpha^{-2}(z-\zeta_2)}{\rho^2+(z-\zeta_2)^2}+\zeta_2\right). \tag{A17}$$

The components of the Jacobians of the isometry maps can be written in matrix form as

$$(J_1)^i_j = \begin{pmatrix} \frac{(z-\zeta_1)^2-\rho^2}{[\rho^2+(z-\zeta_1)^2]^2} & 0 & \frac{-2\rho(z-\zeta_1)}{[\rho^2+(z-\zeta_1)^2]^2} \\ 0 & 1 & 0 \\ \frac{-2\rho(z-\zeta_1)}{[\rho^2+(z-\zeta_1)^2]^2} & 0 & \frac{\rho^2-(z-\zeta_1)^2}{[\rho^2+(z-\zeta_1)^2]^2} \end{pmatrix}, \tag{A18}$$

$$(J_2)^i_j = \begin{pmatrix} \frac{\alpha^{-2}[(z-\zeta_2)^2-\rho^2]}{[\rho^2+(z-\zeta_2)^2]^2} & 0 & \frac{-2\alpha^{-2}\rho(z-\zeta_2)}{[\rho^2+(z-\zeta_2)^2]^2} \\ 0 & 1 & 0 \\ \frac{-2\alpha^{-2}\rho(z-\zeta_2)}{[\rho^2+(z-\zeta_2)^2]^2} & 0 & \frac{\alpha^{-2}[\rho^2-(z-\zeta_2)^2]}{[\rho^2+(z-\zeta_2)^2]^2} \end{pmatrix}. \tag{A19}$$

For completeness, the dimensionless form for the "imaged" scale factors (A5)–(A6) are

$$F_1^n = \begin{cases} \left.\frac{F_1^{n-1}}{\rho^2+(z-\zeta_1)^2}\right|_{(x_1^{n-1})} & \text{for } n \text{ odd}, \\ \left.\frac{\alpha^{-2}F_1^{n-1}}{\rho^2+(z-\zeta_2)^2}\right|_{(x_1^{n-1})} & \text{for } n \text{ even}, \\ 1 \text{ for } n = 0, \end{cases} \tag{A20}$$

$$F_2^n = \begin{cases} \left.\frac{\alpha^{-2}F_2^{n-1}}{\rho^2+(z-\zeta_2)^2}\right|_{(x_2^{n-1})} & \text{for } n \text{ odd}, \\ \left.\frac{F_2^{n-1}}{\rho^2+(z-\zeta_1)^2}\right|_{(x_2^{n-1})} & \text{for } n \text{ even}, \\ 1 \text{ for } n = 0. \end{cases} \tag{A21}$$

With the definitions given above, the components of the inversion-symmetric extrinsic curvature can be computed to arbitrary accuracy. However, because of the use of cylindrical coordinates, there are complications in obtaining accurate and smooth numerical values of the square of the extrinsic curvature. The square of the extrinsic curvature can be written in dimensionless form as

$$\begin{aligned} a_1^2 \bar{A}_{ij}\bar{A}^{ij} = &\left\{\left[\mathcal{R}^{\pm} \circ \left(\frac{\hat{A}}{a_1}\right)\right]_{\rho\rho}\right\}^2 + \left\{\frac{1}{\rho^2}\left[\mathcal{R}^{\pm} \circ \left(\frac{\hat{A}}{a_1}\right)\right]_{\phi\phi}\right\}^2 + \left\{\left[\mathcal{R}^{\pm} \circ \left(\frac{\hat{A}}{a_1}\right)\right]_{zz}\right\}^2 \\ &+2\left\{\left[\mathcal{R}^{\pm} \circ \left(\frac{\hat{A}}{a_1}\right)\right]_{\rho z}\right\}^2 + 2\left\{\frac{1}{\rho}\left[\mathcal{R}^{\pm} \circ \left(\frac{\hat{A}}{a_1}\right)\right]_{\rho\phi}\right\}^2 + 2\left\{\frac{1}{\rho}\left[\mathcal{R}^{\pm} \circ \left(\frac{\hat{A}}{a_1}\right)\right]_{\phi z}\right\}^2. \end{aligned} \tag{A22}$$

It is clear that care must be taken in computing the second, fifth, and sixth terms on the right-hand side of (A22) so as not to encounter roundoff and division by zero errors as the $\rho = 0$ axis is approached. The second term is easily handled by the fact that $\bar{A}_{ij}$ is traceless. The last two terms cannot be handled so easily. The proper evaluation of these terms depends on the fact that in axisymmetry and cylindrical coordinates, the imaging transformation does not mix the linear and angular momentum terms. That is, the evaluation of

$$\frac{1}{\rho}\left[\mathcal{R}^{\pm} \circ \left(\frac{\hat{A}}{a_1}\right)\right]_{\rho\phi} \quad \text{and} \quad \frac{1}{\rho}\left[\mathcal{R}^{\pm} \circ \left(\frac{\hat{A}}{a_1}\right)\right]_{\phi z} \tag{A23}$$

depends only on $\hat{A}_{\rho\phi}$ and $\hat{A}_{\phi z}$. Looking at (A14) and (A15), we see that both terms contain overall factors of ρ. This indicates that the factors of $1/\rho$ should be "commuted" with the inversion operator. Consider the nth term in the expansion for the first expression in (A23):

$$\begin{aligned} &\frac{1}{\rho}F_1^n\left[(M_1^n)_i^k\left(\hat{A}_{k\ell}\right)_{(x_1^n)}(M_1^n)_j^\ell\right]_{\rho\phi} \\ &+\frac{1}{\rho}F_2^n\left[(M_2^n)_i^k\left(\hat{A}_{k\ell}\right)_{(x_2^n)}(M_2^n)_j^\ell\right]_{\rho\phi}. \end{aligned} \tag{A24}$$

If we denote the ρ component of x_α^n as ρ_α^n, then it is straightforward to verify that

$$\frac{1}{\rho} = \frac{F_\alpha^n}{\rho_\alpha^n}, \tag{A25}$$

and so (A24) can be rewritten as

$$\begin{aligned} &(F_1^n)^2\left[(M_1^n)_i^k\left(\frac{\hat{A}_{k\ell}}{\rho}\right)_{(x_1^n)}(M_1^n)_j^\ell\right]_{\rho\phi} \\ &+(F_2^n)^2\left[(M_2^n)_i^k\left(\frac{\hat{A}_{k\ell}}{\rho}\right)_{(x_2^n)}(M_2^n)_j^\ell\right]_{\rho\phi}, \end{aligned} \tag{A26}$$

which is completely regular as the $\rho = 0$ axis is approached. The second expression in (A23) can be handled in exactly the same manner.

APPENDIX B: NUMERICAL EVALUATION OF MISNER'S SOLUTION TO THE HAMILTONIAN CONSTRAINT

Misner has given a formal, inversion-symmetric solution for the Hamiltonian constraint in the case of N holes at a moment of time symmetry [4]. In the case of two equal-sized holes, Lindquist [19] has given an explicit, analytic form for the formal solution in terms of an infinite series in bispherical coordinates. In this appendix, I outline a simple method of evaluating Misner's solution in the case of two, arbitrary sized holes.

For any number of holes, Misner's solution can be expressed in terms of a scalar imaging operator $\mathcal{N}_\alpha$ acting through the αth hole. This operator is defined by the two conditions

$$\mathcal{N}_\alpha \circ \psi(x) \equiv \frac{a_\alpha}{r_\alpha}\psi[J_\alpha(x)] \quad \text{and} \quad \mathcal{N}_\alpha \circ 1 \equiv \frac{a_\alpha}{r_\alpha}. \tag{B1}$$

The general N hole solution is represented formally by

$$\psi(x) = 1 + \sum_{\{\alpha_i\}} \left(\prod_{i=1}^{m} \mathcal{N}_{\alpha_i} \right), \tag{B2}$$

where the notation is as described for Eq. (15). For the case of two holes, a straightforward but tedious calculation reduces (B2) to

$$\psi(x) = 1 + \sum_{n=1}^{\infty} \left(\frac{W_1^n}{r_1^n} + \frac{W_2^n}{r_2^n} \right), \tag{B3}$$

based on the following recursively defined quantities:

$$\zeta_1^n \equiv \begin{cases} \frac{1}{\zeta_1^{n-1} - \zeta_1} + \zeta_1 & \text{for } n \text{ odd}, \\ \frac{\alpha^{-2}}{\zeta_1^{n-1} - \zeta_2} + \zeta_2 & \text{for } n \text{ even}, \\ \zeta_1 \text{ for } n = 1, \end{cases} \tag{B4}$$

$$\zeta_2^n \equiv \begin{cases} \frac{\alpha^{-2}}{\zeta_2^{n-1} - \zeta_2} + \zeta_2 & \text{for } n \text{ odd}, \\ \frac{1}{\zeta_2^{n-1} - \zeta_1} + \zeta_1 & \text{for } n \text{ even}, \\ \zeta_2 \text{ for } n = 1, \end{cases} \tag{B5}$$

$$W_1^n \equiv \begin{cases} \frac{W_1^{n-1}}{|\zeta_1^{n-1} - \zeta_1|} & \text{for } n \text{ odd}, \\ \frac{\alpha^{-1} W_1^{n-1}}{|\zeta_1^{n-1} - \zeta_2|} & \text{for } n \text{ even}, \\ 1 \text{ for } n = 1, \end{cases} \tag{B6}$$

$$W_2^n \equiv \begin{cases} \frac{\alpha^{-1} W_2^{n-1}}{|\zeta_2^{n-1} - \zeta_2|} & \text{for } n \text{ odd}, \\ \frac{W_2^{n-1}}{|\zeta_2^{n-1} - \zeta_1|} & \text{for } n \text{ even}, \\ 1 \text{ for } n = 1, \end{cases} \tag{B7}$$

$$r_1^n \equiv \sqrt{\rho^2 + (z - \zeta_1^n)^2}, \tag{B8}$$

$$r_2^n \equiv \sqrt{\rho^2 + (z - \zeta_2^n)^2}. \tag{B9}$$

ζ_1 and ζ_2 are defined in (A7), and α is defined in (27).

The series expansion for the conformal factor (B3) differs from the expansion for the extrinsic curvature (19) in the crucial point that each term in (B3) is evaluated at the same spatial point. In (19), the point of evaluation for each term is imaged. This complication was necessary in the case of the extrinsic curvature in order to make the solution tractable. Since the position dependence of (B3) is not imaged, the series expansion can be used directly in the integrals for the multipole moments (24) and (25). The results for the total ADM energy and dipole moment are

$$\frac{E}{a_1} = 2 \sum_{n=1}^{\infty} (W_1^n + W_2^n), \tag{B10}$$

$$\frac{d_z}{a_1^2} = 2 \sum_{n=1}^{\infty} (W_1^n \zeta_1^n + W_2^n \zeta_2^n). \tag{B11}$$

APPENDIX C: ČADEŽ COORDINATES

Čadež coordinates are defined in terms of a complex-plane transformation. Letting the base coordinate system be cylindrical coordinates, the complex variable ζ is defined as

$$\zeta \equiv z + i\rho. \tag{C1}$$

The Čadež coordinates are defined as the real and imaginary parts of a complex function $\chi(\zeta)$. Specifically,

$$\eta(\rho, z) \equiv \mathrm{Re}\chi(\zeta) \quad \text{and} \quad \xi(\rho, z) \equiv \mathrm{Im}\chi(\zeta). \tag{C2}$$

Defined in this way, the coordinate system is guaranteed to be orthogonal everywhere that χ is analytic. The explicit form of the complex function χ is taken to be

$$\chi(\zeta) \equiv C_0^+ \ln(\zeta - \zeta^+) + C_0^- \ln(\zeta - \zeta^-) + \sum_{n=1}^{\infty} [C_n^+ (\zeta - \zeta^+)^{-n} + C_n^- (\zeta - \zeta^-)^{-n}]. \tag{C3}$$

The coefficients $C_i^\pm$ are real scalars, and the two complex parameters $\zeta^\pm$ fix the locations of the two holes and are defined by

$$\zeta^+ \equiv \zeta_1 + i0 \quad \text{and} \quad \zeta^- \equiv \zeta_2 + i0, \tag{C4}$$

in terms of the definitions in (A7) and (27) and (28).

To see the general behavior of this transformation, consider the limit that $|\zeta|$ is large compared to $|\zeta^+|$ and $|\zeta^-|$. In this case, the coordinate transformations become

$$\eta(\rho, z) \approx (C_0^+ + C_0^-) \ln \sqrt{\rho^2 + z^2}, \tag{C5}$$

$$\xi(\rho, z) \approx (C_0^+ + C_0^-) \arg(\zeta). \tag{C6}$$

We are free to scale the Čadež coordinates so that $C_0^+ + C_0^- = 1$ and, in this limit, η is simply a logarithmically scaled, spherical-polar radial coordinate and ξ is simply the spherical-polar colatitude coordinate.

The remaining coefficients are fixed by the demand that the spherical throats be surfaces of constant η. In terms of the complex variable ζ, the two sets of points constituting the throats can be parametrized by $\theta^\pm$ as

$$\zeta(\theta^+) \equiv \zeta^+ + \cos\theta^+ + i \sin\theta^+, \tag{C7}$$

$$\zeta(\theta^-) \equiv \zeta^- + \alpha^{-1}(\cos\theta^- + i \sin\theta^-), \tag{C8}$$

where $0 \le \theta^\pm \le \pi$. The coefficients $C_i^\pm$ are then fixed by

$$\eta^+ = \mathrm{Re}\chi[\zeta(\theta^+)] \quad \text{and} \quad \eta^- = \mathrm{Re}\chi[\zeta(\theta^-)], \tag{C9}$$

where $\eta^\pm$ are the coordinate values of the Čadež coordinate η for each of the throats (which can be freely chosen and will be discussed further below) and with the constraint that $C_0^+ + C_0^- = 1$. In practice, the infinite series (C3) is truncated and the two equations (C9) are evaluated on a large set of points on (C7) and (C8). This yields a set of equations which can be used to fix the $C_i^\pm$ coefficients numerically by a linear least-squares fit.

While the coordinate transformation from cylindrical to Čadež coordinates is easily obtained from (C3), the inverse transformation from Čadež to cylindrical coordinates has no simple expression of which I am aware. Determining the cylindrical coordinate location of a given Čadež coordinate pair (η, ξ) must be accomplished by numerical means and can be computed via Newton's method generalized for complex functions.

Because of the behavior demanded in the coordinate system around the throats and built in at large distances,

there is necessarily a critical point in the complex transformation (C3). This critical point is, in fact, a saddle-point singularity of the coordinate system and will be located somewhere on the $\rho = 0$ axis between the two throats. The exact location will be determined by the choices made for the values of $\eta^{\pm}$. In fact, the freedom to choose $\eta^{\pm}$ is used to position the singularity at some desired location. Given choices for $\eta^{\pm}$, the actual position of the singular point can be determined by numerically solving the critical point equation $\partial\chi/\partial\zeta = 0$ (again by Newton's method).

The final freedom in specifying the Čadež coordinate system is ultimately determined by the demands of the discretization near the singular point as described in Sec. VI. From Eq. (51c) we demand that

$$\frac{\eta_s - \eta^+}{\eta_s - \eta^-} = \frac{\mathcal{I}^+ + \frac{1}{2}}{\mathcal{I}^- + \frac{1}{2}}, \tag{C10}$$

where $\mathcal{I}^{\pm}$ are integers defined in (51b) and η_s is the η coordinate value of the singular point. This demand can be satisfied iteratively by making initial guesses for $\eta^{\pm}$, solving for the Čadež coefficients, and determining an initial value for η_s. Next, if (C10) is not satisfied, assume $\eta^+ \to \eta^+ + \varepsilon$ and $\eta^- \to \eta^- - \varepsilon$. Inserting these into (C10) and solving for ε gives new guesses for $\eta^{\pm}$ and the cycle continues until (C10) is satisfied. This procedure has proven to be rapidly convergent.

APPENDIX D: MINIMAL SURFACES AND APPARENT HORIZONS

For the case of a single inversion-symmetric black hole with linear and/or angular momenta, it has been shown that if the extrinsic curvature satisfies isometry condition (6) with a minus sign, then the minimal surface and the apparent horizon coincide [12]. If the isometry condition with a plus sign is satisfied, then the minimal surface and apparent horizon do not coincide except in the degenerate case of time symmetry. In this appendix, I will show that in initial-data sets constructed in accord with the conformal-imaging approach, the minimal surface for each hole is always a trapped surface, regardless of the number of holes, if the extrinsic curvature satisfies condition (6) with the minus sign.

The trapped-surface equation can be written as [12]

$$D_i s^i - \tfrac{2}{3}K + A_{ij}s^i s^j = 0, \tag{D1}$$

where s^i is the outward-pointing, spacelike unit-normal vector to the trapped surface and A_{ij} is the trace-free part of the physical extrinsic curvature. From (6) we find that A_{ij} must satisfy

$$A_{ij}(x) = \pm (J_\alpha)_i^k (J_\alpha)_j^\ell A_{k\ell}[J_\alpha(x)]. \tag{D2}$$

In the conformally flat background space, the unit normal to a sphere centered around the αth hole is n_α^i. We find, then, that the unit normal to the αth minimal surface in the physical space is

$$\tilde{s}_\alpha^i = \psi^{-2} n_\alpha^i, \tag{D3}$$

with the understanding that we are restricted to $r_\alpha = a_\alpha$.

Consider now the third term in (D1) where we substitute the unit normal to the αth minimal surface for the normal to the trapped surface:

$$\tilde{s}_\alpha^i \tilde{s}_\alpha^j A_{ij}(x) = \pm \tilde{s}_\alpha^i (J_\alpha)_i^k \tilde{s}_\alpha^j (J_\alpha)_j^\ell A_{k\ell}[J_\alpha(x)]. \tag{D4}$$

In terms of the Cartesian coordinate definition of the isometry maps given in (7), we find that

$$\begin{aligned}\tilde{s}_\alpha^i (J_\alpha)_i^j &= \psi^{-2} n_\alpha^i \left(\frac{a_\alpha}{r_\alpha}\right)^2 (\delta_i^j - 2n_\alpha^j n_i^\alpha) \\ &= -\left(\frac{a_\alpha}{r_\alpha}\right)^2 \tilde{s}_\alpha^j.\end{aligned} \tag{D5}$$

We recall now that the αth minimal surface is a fixed-point set of the αth isometry map. We have, therefore, $J_\alpha(x) = x$ (and $r_\alpha = a_\alpha$), and so Eq. (D4) becomes

$$\tilde{s}_\alpha^i \tilde{s}_\alpha^j A_{ij}(x) = \pm \tilde{s}_\alpha^i \tilde{s}_\alpha^j A_{ij}(x). \tag{D6}$$

We conclude, therefore, that if isometry condition (6) on the extrinsic curvature is satisfied with the minus sign, then

$$\tilde{s}_\alpha^i \tilde{s}_\alpha^j A_{ij}(r_\alpha = a_\alpha) = 0. \tag{D7}$$

But we know that $D_i \tilde{s}_\alpha^i = 0$ because $\tilde{s}_\alpha^i$ is the unit normal to a minimal surface. We also have $K = 0$ by construction in the conformal-imaging approach. We, therefore, find that $\tilde{s}_\alpha^i$ satisfies the trapped-surface equation (D1) and so the minimal surface is a trapped surface (and an apparent horizon if there are no other trapped surfaces surrounding it) if the extrinsic curvature satisfies isometry condition (6) with a minus sign.

[1] A. Čadež, Ph.D. dissertation, University of North Carolina, 1971.

[2] L. L. Smarr, A. Čadež, B. DeWitt, and K. Eppley, Phys. Rev. D **14**, 2443 (1976).

[3] L. L. Smarr, in *Eighth Texas Symposium on Relativistic Astrophysics*, Boston, Massachusetts, 1976, edited by M. D. Papagiannis, Ann. N.Y. Acad. Sci. Vol. 302 (The New York Academy of Sciences, New York, 1977).

[4] C. W. Misner, Ann. Phys. (N.Y.) **24**, 102 (1963).

[5] J. W. York, Jr., in *Sources of Gravitational Radiation*, edited by L. L. Smarr (Cambridge University Press, London, 1979).

[6] J. Bowen, Gen. Relativ. Gravit. **11**, 227 (1979).

[7] J. Bowen and J. W. York, Jr., Phys. Rev. D **21**, 2047 (1980).

[8] J. Bowen, Gen. Relativ. Gravit. **14**, 1183 (1982).

[9] A. D. Kulkarni, L. C. Shepley, and J. W. York, Jr., Phys. Lett. **96A**, 228 (1983).

[10] J. W. York, Jr. and T. Piran, in *Spacetime and Geometry: The Alfred Schild Lectures*, edited by R. Matzner and L. Shepley (University of Texas Press, Austin, 1982).

[11] M. Choptuik and W. G. Unruh, Gen. Relativ. Gravit. **18**, 813 (1986).

[12] G. B. Cook and J. W. York, Jr., Phys. Rev. D **41**, 1077

(1990).
[13] J. Bowen, J. D. Rauber, and J. W. York, Jr., Class. Quantum Grav. **1**, 591 (1984).
[14] J. D. Rauber, Ph.D. dissertation, University of North Carolina, 1985.
[15] J. Thornburg, Class. Quantum Grav. **4**, 1119 (1987).
[16] G. Cook and A. Abrahams (unpublished).
[17] R. Arnowitt, S. Desser, and C. W. Misner, in *Gravitation: An Introduction to Current Research*, edited by L. Witten (Wiley, New York, 1962).
[18] A. Einstein and N. Rosen, Phys. Rev. **48**, 73 (1935).
[19] R. W. Lindquist, J. Math. Phys. **4**, 938 (1963).
[20] A. D. Kulkarni, J. Math. Phys. **25**, 1028 (1984).
[21] G. B. Cook, Ph.D. dissertation, University of North Carolina, 1990.
[22] J. E. Dendy, Jr., J. Comput. Phys. **48**, 366 (1982).
[23] D. W. Hobill (private communication).
[24] D. Christodoulou, Phys. Rev. Lett. **25**, 1596 (1970).
[25] S. W. Hawking, Phys. Rev. Lett. **26**, 1344 (1971).
[26] R. M. Wald, Phys. Rev. D **6**, 406 (1972).